White Rose Research Online

eprints@whiterose.ac.uk
https://eprints.whiterose.ac.uk
Universities of Leeds, Sheffield and York

Deposited via The University of Sheffield.

White Rose Research Online URL for this paper:
https://eprints.whiterose.ac.uk/id/eprint/243820/

Version: Accepted Version

**Article:**

Guo, K., Zhang, J., Gu, J. et al. (2026) Transformation induced plasticity and hetero-deformation induced strengthening enable superior strength-ductility combination of a novel Ni-Mn-Ti-Fe-Co eutectic high entropy alloy. Journal of Alloys and Compounds, 1070. 188718. ISSN: 0925-8388

https://doi.org/10.1016/j.jallcom.2026.188718

© 2026 The Authors. Except as otherwise noted, this author-accepted version of a journal article published in Journal of Alloys and Compounds is made available via the University of Sheffield Research Publications and Copyright Policy under the terms of the Creative Commons Attribution 4.0 International License (CC-BY 4.0), which permits unrestricted use, distribution and reproduction in any medium, provided the original work is properly cited. To view a copy of this licence, visit http://creativecommons.org/licenses/by/4.0/

**Reuse**

This article is distributed under the terms of the Creative Commons Attribution (CC BY) licence. This licence allows you to distribute, remix, tweak, and build upon the work, even commercially, as long as you credit the authors for the original work. More information and the full terms of the licence here: https://creativecommons.org/licenses/

**Takedown**

If you consider content in White Rose Research Online to be in breach of UK law, please notify us by emailing eprints@whiterose.ac.uk including the URL of the record and the reason for the withdrawal request.

UNIVERSITY OF LEEDS
University of Sheffield
UNIVERSITY of York

# Transformation induced plasticity and hetero-deformation induced strengthening enable superior strength-ductility combination of a Novel Ni-Mn-Ti-Fe-Co eutectic high entropy alloy

Keliang Guo [a], Jinyu Zhang [a,b], Jianglong Gu [c], Jing Bai [a,b] *, Yu Zhang [a], Nicola Morley [d], Jing Yang [b], Qingshuang Ma [b], Qiuzhi Gao [b], Liang Zuo [a]

[a] Key Laboratory for Anisotropy and Texture of Materials (Ministry of Education), School of Material Science and Engineering, Northeastern University, Shenyang 110819, China

[b] Key Laboratory of Dielectric and Electrolyte Functional Material Hebei Province, School of Resources and Materials, Northeastern University at Qinhuangdao, Qinhuangdao 066004, PR China

[c] State Key Laboratory of Metastable Materials Science and Technology, Yanshan University, Qinhuangdao 066004, China

[d] Department of Material Science and Engineering, University of Sheffield, Sheffield, S1 3JD, UK

*Corresponding author: baijing@neuq.edu.cn

## Abstract

Achieving an optimal balance between ductility and strength in high-entropy alloys (HEAs) remains a significant challenge. In this study, a series of eutectic high-entropy alloys (EHEAs) with the nominal composition of $Ni_{35}Mn_{25}Ti_{18\text{-}x}Fe_{12+x}Co_{10}$ ($x$ = 0, 2, 3, 4, 6; at.%) were prepared by arc melting under an argon protection. All alloys exhibit a heterogeneous microstructure composed of FCC and B2 dual-phase structures, which undergo sequential phase evolution: from dual- phase to hypoeutectic, followed by near-eutectic, and ultimately hypereutectic with increasing Fe content. Notably, the $Ni_{35}Mn_{25}Ti_{18\text{-}x}Fe_{12+x}Co_{10}$ alloy exhibits a nearly complete lamellar eutectic structure, achieving an exceptional combination of strength and ductility. All alloys exhibit a yield strength exceeding 950 MPa. In particular, the hypereutectic alloy maintains a yield strength of 990 MPa while exhibiting an excellent fracture strength of 2417 MPa and a fracture strain of 30.2%. The superior mechanical properties of these alloys can be attributed to transformation-induced plasticity (TRIP) via the B2 → $L1_0$ martensitic transformation during deformation, as well as hetero-deformation induced (HDI) strengthening between the soft and hard phases. These findings provide critical insights for designing HEAs with optimized strength-ductility synergy.

**Keywords:** Eutectic high entropy alloy; TRIP effect; HDI strengthening; Strength-ductility combination

# 1. Introduction

Alloy design serves as a crucial approach for enhancing the mechanical properties of metallic materials. In contrast to traditional alloys, which are typically produced by doping a primary metal with minor alloying elements, high-entropy alloys (HEAs) are composed of four or more principal elements with concentrations ranging from 5 at.% to 35 at.%. Since the concept was independently proposed by Yeh et al. [1] and Cantor et al.[2] in 2004, HEAs have emerged as a research hotspot in the field of metallic materials due to their distinctive “high-entropy effect”. This effect suppresses the formation of brittle intermetallic compounds and facilitates the development of simple solid-solution phases, such as face-centered cubic (FCC), body-centered cubic (BCC), or hexagonal close-packed (HCP) structures. Consequently, these microstructural features endow HEAs with exceptional mechanical properties, including high strength, high hardness, superior corrosion resistance, and excellent high-temperature stability. These characteristics highlight the potential of HEAs to serve as promising candidates for replacing traditional alloys in extreme environments, such as deep-space exploration and nuclear reactor applications [3-6]. However, the mechanical properties of single-phase HEAs are often limited by the inefficiency of solid-solution strengthening [7], leading to a persistent strength-ductility trade-off. Specifically, while FCC phases exhibit excellent ductility, their strength remains insufficient [8], whereas BCC phases achieve significant strength enhancement through mechanisms such as dislocation hardening, but at the expense of plasticity [9]. This intrinsic conflict has prompted researchers to explore multiphase structural design strategies. To overcome these limitations, a concept called eutectic high/medium entropy alloys (EH/MEAs) was proposed by Lu et al. [10]. EH/MEAs, by forming dual-phase or multiphase heterogeneous structures (e.g., FCC/BCC lamellar structures), achieve a synergistic enhancement of both strength and ductility through phase cooperation effects [11-15]. However, while current research has focused on macroscopic phase design, challenges remain in understanding and controlling synergistic deformation mechanisms at the microscale. How to activate multiscale cooperative deformation mechanisms-such as transformation-induced plasticity (TRIP) and hetero-deformation induced (HDI) strengthening-through precise microstructural engineering remains a critical unresolved challenge in this field. Studies have demonstrated that the TRIP effect enhances work-hardening ability through stress-induced martensitic transformations [16, 17]. During deformation, this mechanism not only delays local temperature rise by releasing latent heat, but also impedes dislocation slip via newly formed martensite interfaces, thereby significantly improving strain hardening. For instance, in FeCoCrNiVSi-based HEAs, the synergistic grain refinement and TRIP effect result in an excellent combination of yield strength (1230 MPa) and ductility (~65%) [18]. Li et al. [19] developed a transformation-induced plasticity-assisted dual-phase HEA (TRIP-DP-HEA) with a composition of $Fe_{50}Mn_{30}Co_{10}Cr_{10}$, in which martensitic transformation is introduced during deformation, leading to improved strength and plasticity. In FCC alloys, the formation of heterogeneous structures can effectively activate HDI strengthening and work hardening [20-23]. Based on their characteristic length scales, heterostructures can be mainly categorized into three types: grain inhomogeneity at the micron scale, including gradient structures [24-26], lamellar structures [27] and core-shell configurations [28]. The heterostructured materials with superior mechanical properties adhere to a fundamental principle: soft zones are constrained by hard zones. During their cooperative deformation process, strain gradients mediated by geometrically necessary dislocations (GNDs) develop near the soft/hard interfaces, resulting in additional strengthening and work hardening of the bulk material [21].

Moreover, due to their multi-component nature, HEAs usually have abundant substructures, including ordered structures, regional phase separation, and nanoprecipitates [29-32], which can further optimize the mechanical properties of EH/MEAs. For instance, Xiong et al. [33] showed that the fine and coherent ordered $L1_2$ precipitates in the FCC matrix effectively hinder dislocation slip, enhancing the mechanical properties of $AlCoCrFeNi_{2.1}$. Similarly, Jia et al. [34] increased the yield strength of the $Ni_{60-x}Co_xCr_{10}Fe_{10}Al_{18}Mo_2$ alloy by promoting the formation of an FCC phase containing nanoscale $\gamma'$ precipitates through increasing the Ni concentration (while reducing Co content).

This study aims to design a novel Ni-Mn-Ti-Fe-Co eutectic high-entropy alloy with exceptional strength–ductility synergy through a multi-scale microstructural regulation strategy. A five-component eutectic alloy system was successfully fabricated via arc melting, establishing stable interfaces with an FCC/BCC dual-phase lamellar eutectic microstructure. By systematically investigating the underlying deformation mechanisms, this work aims to open a new pathway for overcoming the strength–ductility trade-off in eutectic high-entropy alloys and provide a theoretical basis for developing advanced structural materials with superior mechanical properties.

# 2. Experiment

## 2.1 Materials and methods

Polycrystalline $Ni_{35}Mn_{25}Ti_{18-x}Fe_{12+x}Co_{10}$ ($x$ = 0, 2, 3, 4, 6 at%) alloy ingots were prepared via arc melting in an argon atmosphere using high-purity Ni, Mn, Ti, Fe and Co. To improve compositional homogeneity, each ingot was remelted four times, and electromagnetic stirring was applied to the molten metal during the melting process. Subsequently, the alloy ingot was suction cast into a cylindrical shape with a diameter of approximately 10 mm. The alloy was denoted as Fe12, Fe14, Fe15, Fe16, and Fe18 based on the atom percentage of Fe in the nominal composition. Samples of various sizes were sectioned from the central region of the ingots using a spark wire-cutting machine for subsequent experiments. The microstructure and chemical composition of the alloys were characterized by scanning electron microscopy (SEM, JSM-7001F) equipped with an Oxford electron backscatter diffraction (EBSD) attachment. Samples for EBSD and TEM investigation were prepared by mechanical polishing, followed by electropolishing (electrolyte: 90% ethanol + 10% perchloric acid) at room temperature. Selected area electron diffraction patterns were obtained using a transmission electron microscope (TEM, JEM-2100F) to further determine the crystal structure at room temperature. The TEM sample preparation process was as follows: alloy specimens were first fabricated into disks with a diameter of 3 mm and a thickness of 50–60 μm, and then thinned using a Struers TenuPol-5 automatic electrolytic twin-jet thinning unit with an electrolyte consisting of 90% ethanol and 10% perchloric acid. The crystal structure was analyzed using X-ray diffraction (XRD, Rigaku Smartlab) with Cu-Kα radiation, at a scanning speed of 5°/min, a step size of 0.02° and a scanning range of 20–90°.

Room-temperature compressive properties of the alloys were tested using a universal testing machine (AG-XPlus 50 kN) according to the GB/T 7314-2005 standard. A linear gauge (Mitutoyo LG100-0110) with a resolution of 0.1 μm was employed to record the displacement data during the compressive tests. The specimens for compressive testing were square-shaped (3 × 4 × 6 mm). Some compression tests were performed to failure, while others were interrupted at specific strains to characterize the features of slip trace characteristics and the sub-structural evolution of different HEAs under varying deformation conditions.

## 2.2 Alloy design strategy

This study aims to develop a novel Ni-Mn-Ti-Fe-Co alloy with an excellent strength-ductility synergy. To achieve this goal, the compositional design follows the principles below:

1) Matrix alloy selection: The Ni-Mn-Ti alloy was chosen as the basic alloy.

According to our previous study, this system can form a BCC austenite matrix within a specific composition range, serving as the parent phase for martensitic transformation.

2) Suppression of Laves phase formation: Alloy systems containing Ti and Fe are prone to forming Laves phases, which are hard and brittle and can severely impair the ductility of the material. To avoid the precipitation of Laves phases, Co was selected as one of the co-doping element in this study. The mixing enthalpy between Co and Ti is less negative than that between Fe and Ti, which helps reduce the driving force for the formation of Laves phase. In addition, the suction casting process was employed to increase the cooling rate, thereby inhibiting the nucleation and growth of Laves phases and further suppressing their formation.

3) Valence electron concentration (VEC) control: By adjusting the Fe/Ti ratio, the VEC of the alloy was controlled within the range of 7.83-8.07, which favors the formation of the FCC + B2 dual-phase structure, ultimately yielding an alloy with the desired FCC + B2 phase constitution.

# 3. Results

## 3.1 Microstructure and phase identification: Phase constituent and microstructure of $Ni_{35}Mn_{25}Ti_{18-x}Fe_{12+x}Co_{10}$ HEAs

**Fig. 1** presents the XRD patterns of $Ni_{35}Mn_{25}Ti_{18-x}Fe_{12+x}Co_{10}$ HEAs. In accordance with Bragger diffraction law and the diffraction extinction law, all five alloys consist of two distinct phases: FCC and BCC. Based on the diffraction peak positions. Subsequent studies indicate that the Fe15 alloy possesses the most complete eutectic structure. To reveal the structure–property relationship, a detailed lattice parameter analysis of the Fe15 alloy was conducted. According to the formula for calculating the interplanar spacing of the cubic crystal system, the lattice parameters of the FCC and BCC phases of the Fe15 alloy were calculated to be approximately 3.64 Å and 2.95 Å, respectively.

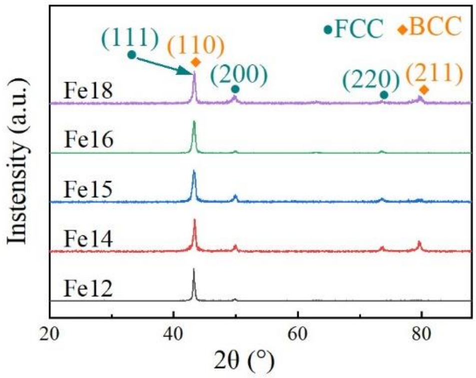


**Fig. 1.** XRD pattern of $Ni_{35}Mn_{25}Ti_{18\text{-}x}Fe_{12+x}Co_{10}$ HEAs.

**Fig. 2** shows back-scattered SEM micrographs of Fe12–Fe18 samples in the as-cast condition. As shown in **Fig. 2**, with increasing Fe content, the volume fraction of the light gray phase decreases, while that of the dark gray phase increases. The $Ni_{35}Mn_{25}Ti_{18\text{-}x}Fe_{12+x}Co_{10}$ alloy system was developed through elemental doping based on the Ni-Mn-Ti system, which features a BCC austenite matrix. Consequently, the present alloy system is expected to retain a BCC austenitic structure as its primary matrix phase. Corresponding to the XRD results (Fig. 1), it can be inferred that the light gray phase is the BCC phase and the dark gray phase is the FCC phase. This result was subsequently confirmed by EBSD analysis (Fig. 5).

The Fe12 alloy exhibits a dual-phase microstructure characterized by numerous elongated FCC precipitates (dark contrast) within the BCC matrix (light contrast). The Fe14 alloy exhibits a hypoeutectic microstructure, as shown in **Fig. 2**(b). This morphology comprises primary BCC dendrite trunks, accompanied by a eutectic structure distributed within the inter-dendritic regions. The volume fraction of the eutectic structure increases with increasing Fe content until reaching 15 at.%. The Fe15 alloy exhibits an almost fully eutectic microstructure, as shown in **Fig. 2**(c). Both the Fe16 and Fe18 alloys display hypereutectic microstructures (**Fig. 2**(d) and (e), respectively), with a progressively increasing amount of proeutectic FCC phase. Notably, the FCC phase in the eutectic structure of Fe15 alloy exhibits the finest and most uniform distribution among all the alloys. As shown in Fig. 2(f), the eutectic structure of the alloy exhibits mainly lamellar and network-like morphologies.

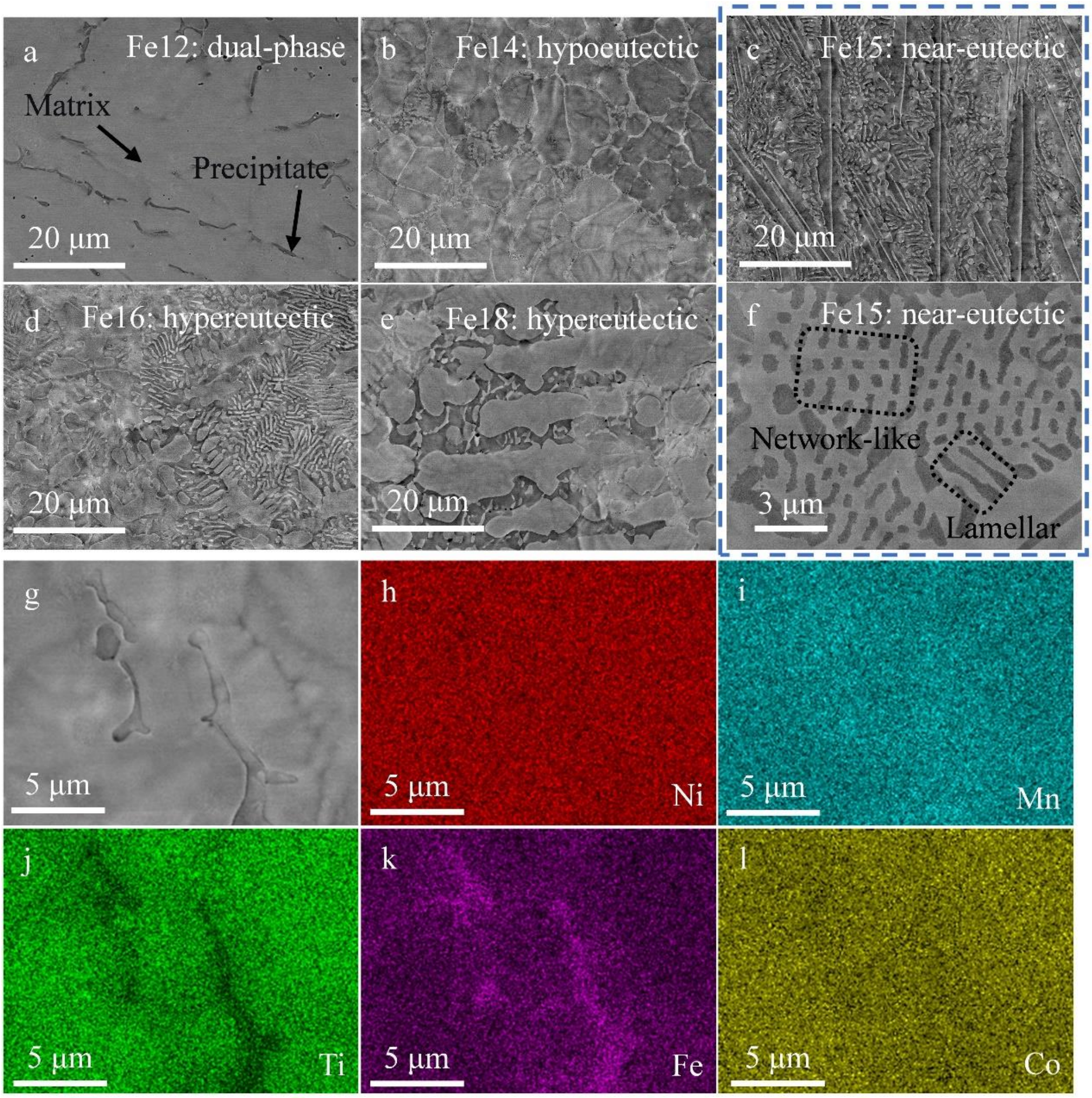


**Fig. 2.** SEM images and EDS results of the $Ni_{35}Mn_{25}Ti_{18\text{-}x}Fe_{12+x}Co_{10}$ alloys. (a) $x$ = 12 (dual-phase); (b) $x$ = 14 (hypoeutectic); (c) $x$ = 15 (near-eutectic); (d) $x$ = 16 (hypereutectic); (e) $x$ = 18 (hypereutectic); (f) $x$ = 15 (near-eutectic), high magnification image; (g)–(k) EDS results of Fe12 alloy.

**Fig. 2**(g) depicts a back-scattered micrograph of the as-cast Fe12 alloy, while **Fig. 2**(h)–(l), displat the elemental mapping images of Ni, Mn, Ti, Fe, and Co, respectively. The matrix exhibits a higher Ti content and a lower Fe content compared to the FCC phase. In contrast, the differences in Ni, Mn, and Co contents between the two phases are relatively minor. This phenomenon is closely related to the nature of the eutectic reaction. During the eutectic reaction, the matrix and the secondary phase form almost simultaneously from the liquid phase, leading to similar elemental concentrations contributing to both phases. This results in comparable contents of Ni, Mn, and Co.

However, due to the different crystal structures of the matrix (BCC) and the second phase (FCC), elemental partitioning occurs, leading to enrichment of certain elements in one phase and depletion in the other. As a result, the distributions of Ti and Fe show significant differences.

To determine the chemical composition of each phase in the alloy, EDS analysis was performed, and the average values from at least three regions were taken to ensure statistical reliability. The results are shown in **Table 1**. As shown in Table 1, the alloy matrix is a Ti-rich phase, while the secondary phase is Fe-rich, which is consistent with the results of the elemental mapping analysis.

**Table 1.** Actual compositions of the matrix and secondary phase determined by EDS for the $Ni_{35}Mn_{25}Ti_{18-x}Fe_{12+x}Co_{10-x}$ ($x$ = 0, 2, 3, 4, 6) alloys.

| Nominal composition | Matrix (at.%) | | | | | Secondary phase (at.%) | | | | |
|---|---|---|---|---|---|---|---|---|---|---|
| | Ni | Mn | Ti | Fe | Co | Ni | Mn | Ti | Fe | Co |
| $Ni_{35}Mn_{25}Ti_{18}Fe_{12}Co_{10}$ | 34.95 | 24.09 | 19.39 | 10.88 | 10.69 | 32.89 | 28.73 | 10.02 | 20.58 | 7.78 |
| $Ni_{35}Mn_{25}Ti_{16}Fe_{14}Co_{10}$ | 34.11 | 23.78 | 17.81 | 12.67 | 11.62 | 34.28 | 25.46 | 11.75 | 19.50 | 9.00 |
| $Ni_{35}Mn_{25}Ti_{15}Fe_{15}Co_{10}$ | 34.71 | 24.16 | 16.60 | 13.80 | 10.73 | 34.15 | 24.63 | 14.20 | 16.98 | 10.04 |
| $Ni_{35}Mn_{25}Ti_{14}Fe_{16}Co_{10}$ | 34.81 | 24.33 | 16.62 | 13.27 | 10.98 | 34.37 | 25.02 | 10.90 | 19.57 | 10.14 |
| $Ni_{35}Mn_{25}Ti_{12}Fe_{18}Co_{10}$ | 35.90 | 24.50 | 16.76 | 13.09 | 9.74 | 33.97 | 24.39 | 9.15 | 21.78 | 10.72 |

To enable a more detailed characterization of the microstructural morphology, secondary electron imaging was performed on the representative Fe14 (hypoeutectic), Fe15 (near-eutectic), and Fe16 (hypereutectic) alloys. Compared with back-scattered electron imaging, secondary electron imaging offers higher-resolution and enhanced three-dimensional surface topographical contrast, facilitating more precise morphological interpretation. **Fig. 3** presents the secondary electron images of the three alloys. Low-magnification images ($a_1$, $b_1$, $c_1$) and high-magnification images ($a_2$, $b_2$, $c_2$) are shown for each composition. In the hypoeutectic Fe14 alloy (**Fig. 3**($a_1$, $a_2$)), the eutectic structure forms an interconnected network extending throughout the austenite matrix, with the second phase closely associated with the eutectic structure, which preferentially forms within matrix regions surrounded by the second phase. In the near-eutectic Fe15 alloy, in addition to the eutectic structure, a continuous bulk matrix is observed, within which elongated second-phase particles are typically interspersed, as shown in **Fig. 3**($b_1$) and ($b_2$). The coexistence of the eutectic structure, bulk matrix, and elongated second phase gives rise to a hierarchical “bionic fishbone-like” herringbone microstructure, characterized by alternating soft and hard layers at the micro-to-nano scale.

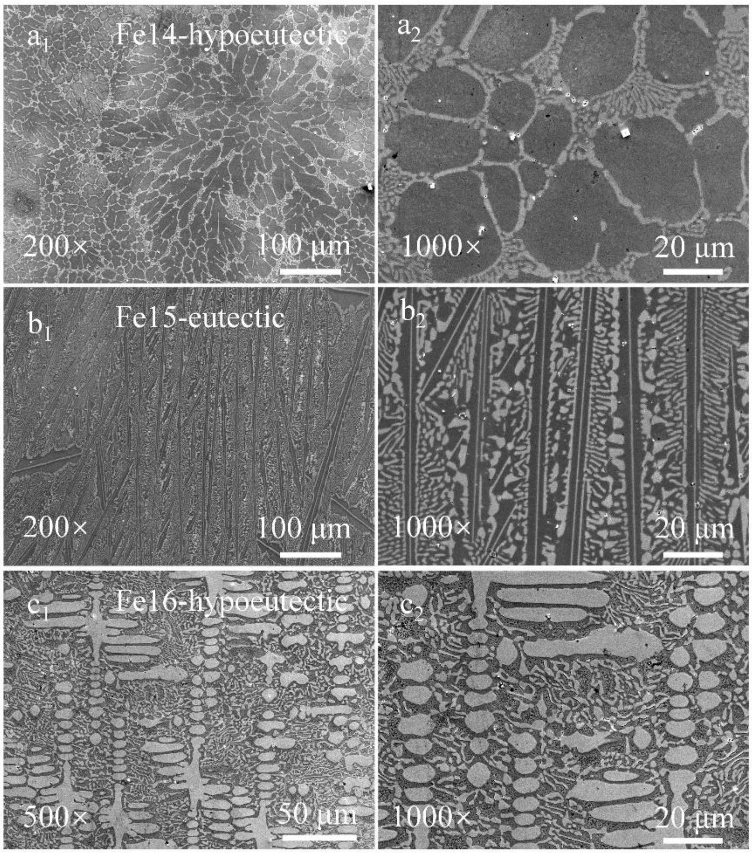


**Fig. 3.** Secondary electron images of hypoeutectic, near-eutectic, and hypereutectic alloys. ($a_1$), ($b_1$), and ($c_1$) are low-magnification images of these alloys, respectively; ($a_2$), ($b_2$), and ($c_2$) are high-magnification images, respectively.

This unique microstructural architecture significantly enhances the ductility of the material. During the initial stages of deformation, microcracks preferentially form in the brittle hard layers, which have limited deformability. Adjacent microstructural features with strong strain-hardening capacity promote local energy dissipation, blunting the crack tips. These microcracks are subsequently confined within individual lamellae, thereby suppressing unstable propagation and catastrophic penetration. The continuous nucleation and growth of microcracks generate extrinsic plasticity, compensating for the inherent brittleness of the hard phase and enabling sustained uniform plastic deformation. The precipitates in the alloy are identified as Fe-rich phase. As the Fe content increases, the volume fraction and average size of the precipitates increase, while the proportion of lamellar and elongated morphologies decreases, and dendritic second phases correspondingly increase, as illustrated in **Fig. 3**($c_1$) and ($c_2$).

To further investigate the microstructure of the HEAs, TEM analysis was conducted on the near-eutectic Fe15 alloy. **Fig. 4** presents the TEM examination of the Fe15 alloy. **Fig. 4**(a) shows a bright field TEM image of the eutectic microstructure, where the BCC (B2) and FCC (γ′) phases are labeled by orange and yellow fonts, respectively. Austenite typically exists in B2 or $L2_1$ structures, which can be identified by TEM through specific zone axes. In **Fig. 4**(b), superlattice diffraction spots corresponding to the (001) plane of the B2 structure (indicated by the red circle) were observed, while no superlattice diffraction spots corresponding to the $L2_1$ structure (111) were detected. This confirms that the austenite in this alloy has a B2 structure. In **Fig. 4**(c), superlattice diffraction spots corresponding to the (100) plane of γ′ (indicated by the red circle) were identified, confirming that the FCC phase in the alloy is the γ′ phase. The γ′ lamellae, which appear in the dark contrast, are approximately 200 nm in thickness and about 500 nm in spacing between them. Compared with B2 (BCC structure), γ′ (FCC structure) possesses more slip systems, which facilitates dislocation motion. Consequently, γ′ phase exhibits lower hardness but enhanced ductility, contributing significantly to the overall ductility of the alloy.

High-resolution transmission electron microscopy (HRTEM) was used to characterize the atomic-scale structure of the B2 phase, γ′ phase, and their interfaces. **Fig. 4**(d) shows the atomic arrangement of the B2 phase viewed along the [111] zone axis, with the corresponding inverse fast Fourier transform (IFFT) image shown in the inset. **Fig. 4**(e) shows the γ' phase structure along the [011] zone axis, with its IFFT image shown in the inset. **Fig. 4**(f) presents the HRTEM image of the B2–γ' interface, which exhibits atomic-scale roughness, a characteristic feature of non-faceted eutectic growth [35]. IFFT analysis confirms the semi-coherent nature of this interface. Based on these observations, we determined the orientation relationship between γ' and B2 phases to be $[111]_{B2}//[011]_{\gamma'}$, which satisfies the classical Kurdjumov–Sachs (K–S) orientation relationship [36].

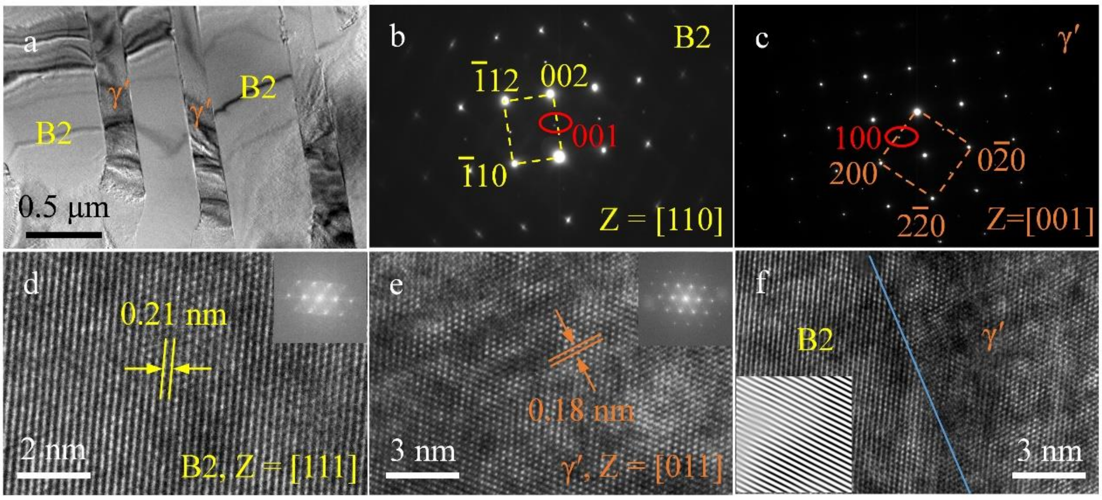


**Fig. 4.** TEM images of the near-eutectic alloy. (a) TEM bright field micrograph; (b) selected area electron diffraction patterns of the B2 phase; (c) selected area electron diffraction patterns of fcc γ′ phase; (d) HRTEM image of B2 phase (inset figure is the IFFT image of the B2 phase); (e) HRTEM image of γ′ phase (inset figures are the IFFT images of γ′ phase); (f) HRTEM image of the B2–γ′ interface (inset figure is the IFFT image of the interface).

## 3.2 Orientation relationship and atomic structure of interfaces

The orientation relationships between phases largely govern the strength and ductility of HEAs. **Fig. 5** presents the EBSD analysis results for Fe14 (hypoeutectic), Fe15 (near-eutectic), and Fe18 (hypereutectic) alloys. From the band contrast (BC) maps (**Fig. 5**($a_1$, $b_1$, $c_1$)) and phase maps (**Fig 5**($a_2$, $b_2$, $c_2$)), the B2 and γ' phases in the selected regions are highlighted in red and yellow, respectively. For the near-eutectic Fe15 alloy (**Fig. 5**($b_1$, $b_2$)), the BC and phase maps confirm that the eutectic structure consists of FCC and BCC phases. **Fig. 5**($b_3$) illustrates the inverse pole figure (IPF) map of the near-eutectic alloy. The orientation of the BCC phase remains stable, while the FCC phase within a single eutectic colony is highly similar but distinct from those in neighboring colonies, which is characteristic of eutectic alloys. Because the eutectic orientation is fixed within a colony, the constituent phases grow cooperatively. **Fig. 5**($b_4$) shows the <111> and <110> pole figures for the BCC and FCC phases, respectively.

The orientation relationship between the FCC and B2 phases is confirmed as $[111]_{BCC}$ // $[011]_{FCC}$, which aligns with the K–S relationship observed in the TEM results.

EBSD analysis of the hypoeutectic (Fe14) and hypereutectic (Fe18) alloys was performed to investigate the orientation relationship between the primary phase and the eutectic structure (**Fig. 5**(a) and (c)). In the hypoeutectic Fe14 alloy (**Fig. 5**($a_1$) and ($a_2$)), the primary phase is BCC, and the eutectic consists of FCC and B2 phases. The IPF map (**Fig. 5**($a_3$)) reveals that the eutectic FCC phase maintains a similar crystallographic orientation to the primary FCC phase. This suggests that during solidification from the interdendritic residual liquid, the eutectic FCC phase preferentially nucleates and undergoes epitaxial growth aligned with the primary FCC phase, thereby preserving a consistent orientation. Pole figures (**Fig. 5**($a_4$)) confirm the absence of a K–S relationship between FCC and B2 in the hypoeutectic alloy.

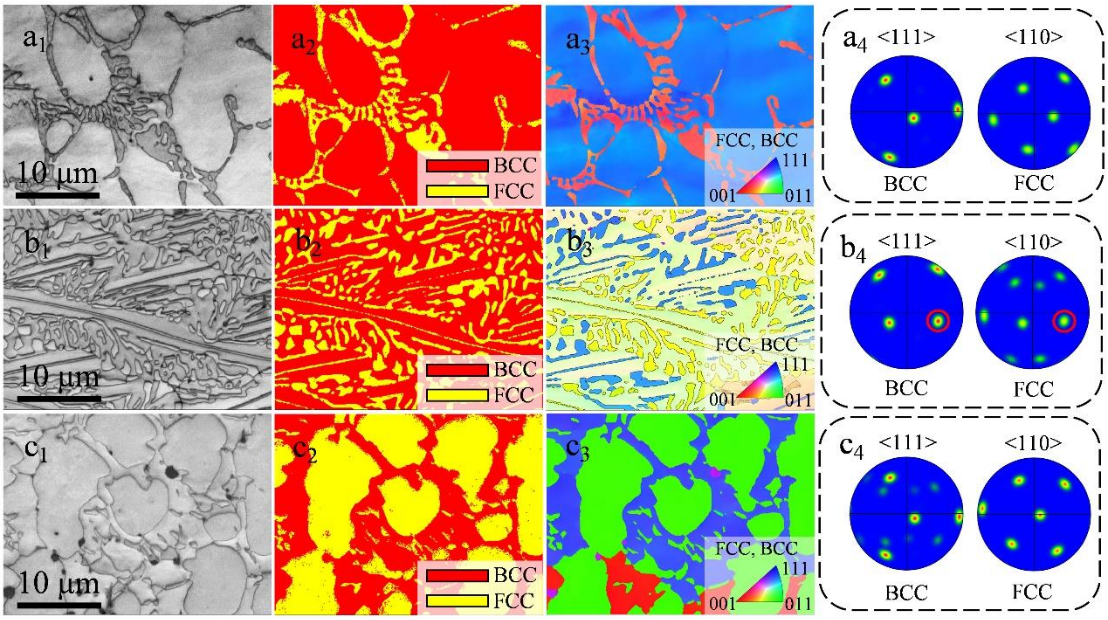


**Fig. 5.** EBSD results of alloys. (a) hypoeutectic alloy; (b) near-eutectic alloy; (c) hypereutectic alloy ((1) BC map; (2) Phase map; (3) IPF map; (4) pole figures of BCC and FCC phases).

**Fig. 5**($c_1$) and ($c_2$) present the BC map and phase map of the hypereutectic Fe18 alloy, respectively, revealing a microstructure composed of primary FCC phase and eutectic structure. The IPF map in **Fig. 5**($c_3$) shows a solidification process analogous to that observed in the hypoeutectic alloy. The eutectic FCC phase grows epitaxially from the primary FCC phase, resulting in closely matched orientations between them. **Fig. 5**($c_4$) shows the <111> and <110> pole figures of the FCC and BCC phases, confirming that the K–S relationship is similarly absent between FCC and B2 phases in the hypereutectic alloy.

In the near-eutectic Fe15 alloy, the K–S orientation relationship is observed between the FCC and B2 phases, whereas this orientation relationship is absent in the hypoeutectic Fe14 and hypereutectic Fe18 alloys. This difference is attributed to the distinct solidification paths. For the near-eutectic Fe15 alloy, both phases grow cooperatively and directly from the liquid. The coupled growth forces the phases to maintain a fixed K–S orientation relationship to minimize the interfacial energy. In contrast, in the hypoeutectic and hypereutectic alloys, solidification begins with the formation of a primary phase (BCC in Fe14 alloy and FCC in Fe16 alloy). When the remaining liquid reaches the eutectic temperature, the eutectic structure nucleates heterogeneously on the existing primary phase. The growth orientation of the eutectic phases is constrained by the primary phase, forcing them to grow in a manner compatible with the primary phase, thereby preventing the formation of the low-energy K–S orientation.

## 3.3 Mechanical properties

**Fig. 6** presents the compressive properties of $Ni_{35}Mn_{25}Ti_{18\text{-}x}Fe_{12+x}Co_{10}$ alloys. **Fig. 6**(a) shows the compressive engineering stress–strain curves for Fe12 to Fe18 alloys. The corresponding yield strength ($\sigma_y$), fracture strength ($\sigma_u$), and fracture strain ($\varepsilon_f$) are plotted as functions of Fe content in **Fig. 6**(b). As the Fe content increases from 12 at.% to 18 at.%, the yield strength decreases from 1268 MPa to 990 MPa. Despite this reduction in yield strength, the alloys still maintain exceptionally high yield strength levels. This phenomenon can be primarily attributed to the cocktail effect. In HEAs, atomic size differences among multiple principal elements induce severe heterogeneous lattice distortion and long-range stress fields, which significantly hinder dislocation motion and thereby enhance the yield strength. This strengthening mechanism is more effective than conventional solid-solution strengthening, enabling the alloy to maintain considerable plasticity while achieving enhanced strength.

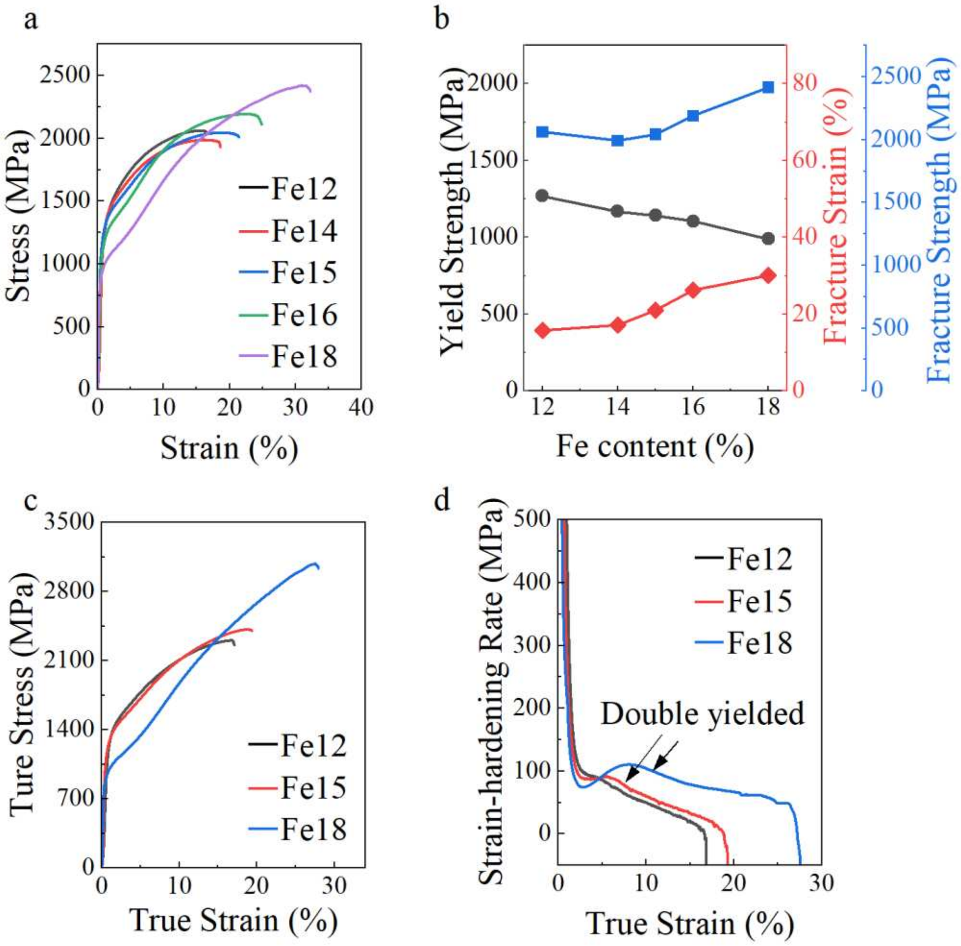


**Fig. 6.** Mechanical properties of $Ni_{35}Mn_{25}Ti_{18-x}Fe_{12+x}Co_{10}$ alloys. (a) Engineering stress-strain curves; (b) Yield Strength, Fracture Strain, and Fracture Strength as a function of Fe content; (c) True stress–strain curves; (d) Strain hardening rate versus true strain curves.

The plasticity of the alloy increases monotonically from 15.7% to 30.2% as the Fe content rises from 12 at.% to 18 at.%. This enhancement is primarily attributed to the increased volume fraction and coarsened size of the γ' phase with higher Fe content, which facilitates relatively easier dislocation motion during deformation and thus improves the ductility. HEAs exhibit an exceptional combination of strength and ductility, necessitating a deeper understanding of the correlation between their microstructural features and deformation mechanisms. Through analysis of true stress–strain curves and strain hardening rate curves, we investigated the macroscopic deformation behavior of these HEAs. **Fig. 6(**d) presents the strain hardening rate curves for three representative HEAs, Fe12, Fe15 and Fe18. The hypereutectic alloys display a four-stage strain hardening behavior: (I) rapid post-yield decline, (II) followed by a fluctuation period, (III) then increases slowly, and (IV) a sharp drop to zero indicating fracture. Notably, the near-eutectic alloy exhibits a fluctuation period, whereas the hypoeutectic alloy lacks both the fluctuation period (stage II) and the gradual ascent phase (stage III).

These fluctuation characteristics correlate strongly with the dual-yield behavior observed in the near-eutectic and hypereutectic alloys [37]. Remarkably, the hypereutectic alloy demonstrates a rapid increase in strain hardening rate before fracture, whereas both hypoeutectic and eutectic alloys fail prematurely. This sustained strain hardening during plastic deformation accounts for the superior strength–toughness combination in hypereutectic alloys, while premature failure explains the relatively lower ductility in hypoeutectic and near-eutectic alloys. As shown in **Fig. 6**, these alloys exhibit both high yield strength and excellent fracture strain, confirming that the designed HEAs with lamellar structures possess outstanding mechanical properties. The compressive stress–strain curves of Fe15, Fe16, and Fe18 alloys demonstrate a distinct "double-yield" deformation behavior. This "double-yield" phenomenon indicates the occurrence of stress-induced martensitic transformation during the deformation process of the near-eutectic and hypereutectic alloys [17].

# 4. Discussion

## 4.1 Transformation-Induced Plasticity

The stress-induced martensitic transformation during the deformation of the near-eutectic alloy can effectively enhance plasticity, a phenomenon known as the TRIP effect [37]. This TRIP effect accounts for the remarkable ductility observed in the near-eutectic alloys. Specifically, the phase transformation occurring in B2 phase during deformation increases both the elastic modulus and hardness, thereby improving resistance to deformation [38]. Consequently, plastic deformation is redistributed to other regions, which suppresses localized strain accumulation. Moreover, the martensitic transformation absorbs elastic strain energy, delaying the rapid propagation of shear bands and inhibiting the initiation of microcrack [39]. This leads to a more homogeneous stress distribution, which enhances the material's capacity for compatible deformation and ultimately improves the overall ductility of near-eutectic alloys.

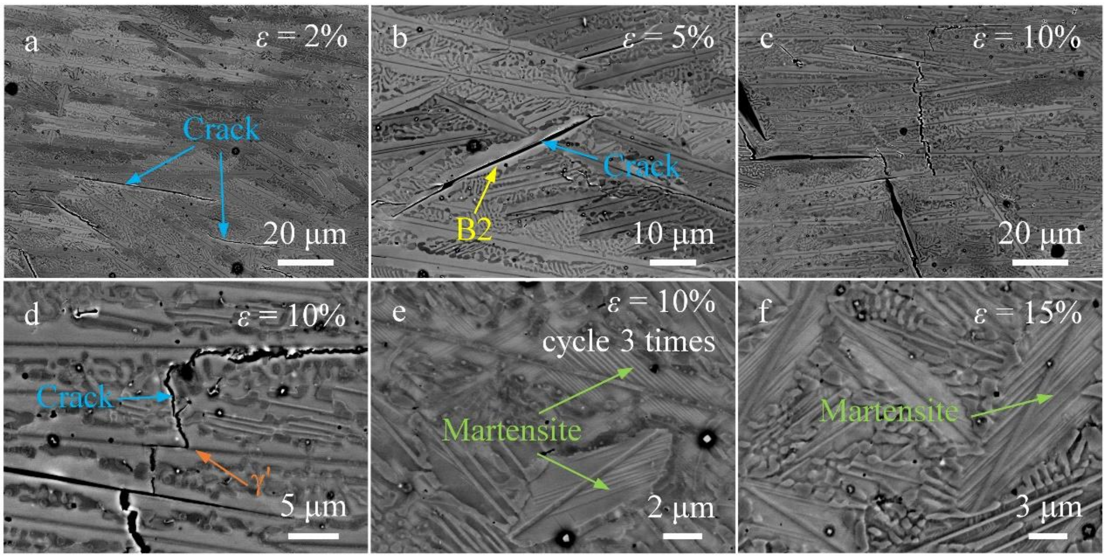


**Fig. 7.** SEM images of Fe15 alloy under different deformation conditions. (a) $\varepsilon$ = 2%; (b) $\varepsilon$ = 5%; (c) $\varepsilon$ = 10%; (d) $\varepsilon$ = 10%, high magnification image; (e) three cycles of 10% strain; (f) $\varepsilon$ = 15%.

**Fig. 7** systematically investigates the microstructural evolution of the Fe15 near-EHEA under different strain ($\varepsilon$) conditions. The results reveal that at relatively low strain ($\varepsilon$ = 2%), microcracks initiate within the alloy, preferentially nucleating at large B2 phases in non-eutectic regions (**Fig. 7**(a) and (b)). As strain increases, the cracks exhibit distinct three-dimensional propagation characteristics, including width expansion and depth penetration (**Fig. 7**(c)). Notably, crack propagation is effectively impeded when encountering γ' phases (**Fig. 7**(d)), demonstrating the superior crack growth resistance of the FCC-structured γ' phases. During deformation, martensite initially forms in the B2 phases of non-eutectic regions after three cycles of 10% strain (**Fig. 7**(e)). Remarkably, when the strain reaches 15%, the alloy directly undergoes martensitic transformation in a single deformation event (**Fig. 7**(f)). This strain-path-dependent phase transformation behavior reveals that cyclic loading reduces the transformation energy barrier through the accumulation of defect energy, whereas high-strain monotonic loading directly satisfies the critical condition for phase transformation. These findings systematically elucidate the underlying microscopic mechanism by which EHEAs achieve a synergistic enhancement of strength and ductility via multi-phase cooperation, from the dual perspectives of crack growth resistance and strain-induced phase transformation.

**Fig.8** presents the EBSD analysis results of the near-eutectic alloy after three cycles of 10% strain deformation. The BC map (**Fig. 8**(a)) and phase map (**Fig. 8**(b)) reveal the spatial distribution of B2 phase (red), γ' phase (yellow), and $L1_0$ martensite (green) in the analyzed region. Notably, the distinct $L1_0$ martensite regions (green) in **Fig. 8**(b) confirm the stress-induced austenite-to-martensite transformation in this alloy, further verifying the activation of the TRIP effect. **Fig. 8**(c) shows the IPF map of the alloy. The orientation of the B2 phase remains stable and consistent with that of the undeformed B2 phase.

The IPF analysis in **Fig. 8**(d) demonstrates that the BCC and FCC phases maintain the $[111]_{BCC} // [011]_{FCC}$ K–S relationship after deformation. This stable crystallographic relationship has a decisive influence on the mechanical properties of the alloy. Specifically, the semi-coherent K–S interface between the FCC and B2 phases facilitates the transmission of approximately 2/3 of dislocations from the <110> slip systems in the FCC phase across the phase boundary [35]. This unique dislocation transmission mechanism significantly enhances slip continuity at γ'–B2 interfaces. During deformation, the continuously maintained K–S relationship not only promotes trans-interface dislocation motion but also effectively alleviates stress concentration at phase boundaries.

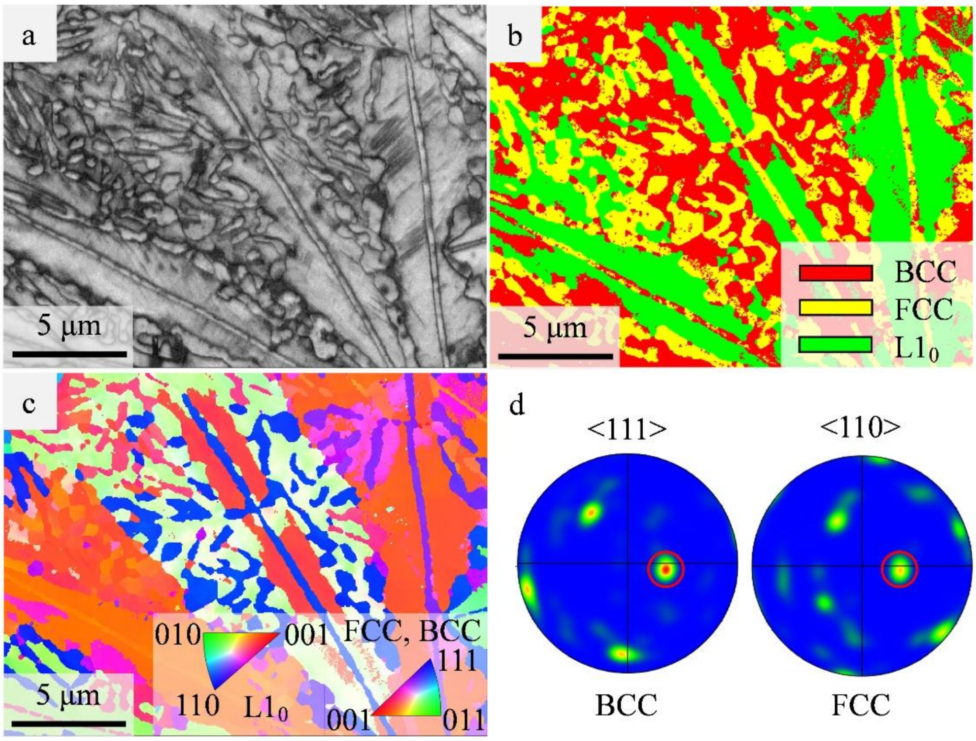


**Fig. 8.** EBSD results of three cycles of 10% strain of Fe15 EHEAs. (a) BC map; (b) Phase map; (c) IPF map; (d) pole figures.

To thoroughly investigate the TRIP effect, this study focuses on the hypereutectic Fe18 alloy, which exhibits the most pronounced TRIP effect. The stress–strain curve is analyzed across distinct deformation stages (**Fig. 9**). The stress–strain curve is analyzed across distinct deformation stages (Fig. 9), allowing the deformation process to be clearly divided into four characteristic stages. Stage I is characterized by coordinated elastic deformation of both the B2 and γ' phases. Stage II features concurrent plastic deformation of the γ' phase and stress-induced transformation of the B2 phase into $L1_0$ martensite. During this stage, the stress–strain curve shows a gradually increasing "stress plateau" [37] , marking the onset of the first yield behavior, which directly corresponds to the initiation of stress-induced $L1_0$ martensitic transformation. Stage III involves plastic deformation of the γ' phase and residual the B2 phase along with continued formation of the $L1_0$ phase. In Stage IV, the material undergoes plastic deformation of the multiphase system and further transformation of the residual B2 phase into the $L1_0$ phase. The second yield behavior is triggered when the critical yield stress of the multiphase system is reached. This systematic analysis of the multistage deformation characteristics provides crucial insights into the underlying mechanism of the TRIP effect in the alloy.

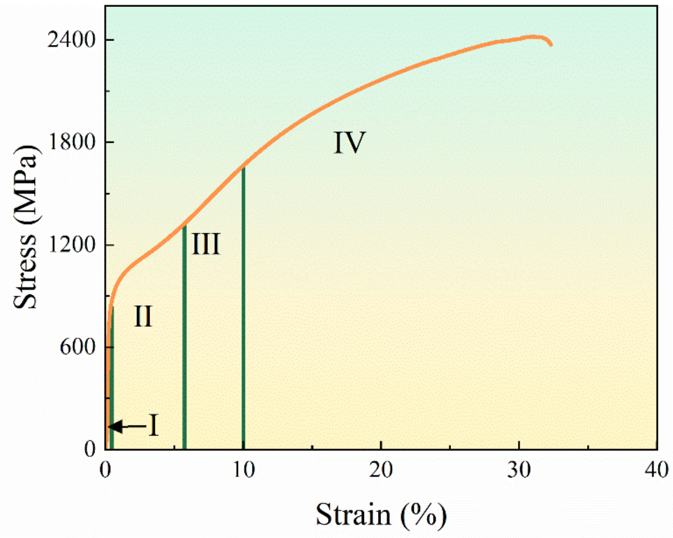


**Fig. 9.** Engineering stress–strain curves of Fe18.

The essence of the TRIP effect lies in the stress-induced transformation of austenite (the B2 phase in this study) into martensite during deformation. This phase transition dissipates energy, introduces plastic deformation, and suppresses localized necking, thereby significantly enhancing the material's uniform elongation and work-hardening capacity. A systematic multistage deformation analysis of the Fe18 alloy reveals that the TRIP effect originates from a coordinated interplay among elastic deformation, plastic slip, stress-induced phase transformation, and post-transformation plasticity. Elucidating the micro-mechanisms governing each deformation stage and their critical transition thresholds provides valuable insights for the design and development of novel TRIP-assisted materials with optimized strength–ductility balance.

## 4.2 HDI strengthening caused by heterostructure

To clarify the contribution of heterogeneous structures to the mechanical properties of materials, we conducted analyses from the perspectives of heterostructure-induced HDI strengthening and work hardening. HDI strengthening has emerged as a key strategy in materials science for simultaneously enhancing both strength and ductility. Heterostructured materials consist of mechanically distinct hard and soft regions, where the pronounced differences in mechanical response lead to deformation incompatibility during plastic straining. When deformation occurs, the soft zones preferentially yield while the hard zones remain relatively resistant, resulting in a strain mismatch that generates GNDs at heterointerfaces [40]. The resulting mutual constraints between regions generate HDI stresses: GND pile-ups in soft domains produce back stresses that impede dislocation motion and increase yield strength, while they generate forward stresses that facilitate dislocation multiplication and motion in hard domains, thereby enhancing work hardening. This synergistic coupling effect significantly improves overall yield strength while providing additional hardening capacity. The appearance of a mechanical hysteresis loop during load-unload-reload (LUR) testing represents a characteristic mechanical response, indicating the significant involvement of GNDs in plastic deformation and the generation of high HDI stress [22, 40]. To elucidate the contribution of HDI stress to mechanical properties, we performed LUR tests on the aforementioned materials. **Fig. 10**(a) presents the true stress-true strain curves for the near-eutectic Fe15 and hypereutectic Fe18 alloys. The HDI stress ($\sigma_{HDI}$) is calculated using the following formula [22, 41]:

$$\sigma_{HDI} = \frac{\sigma_r + \sigma_u}{2} \tag{1}$$

where $\sigma_r$ is the reload yield strength, and $\sigma_u$ is the unload yield strength. **Fig. 10**(b) shows that the mechanical hysteresis loop of the Fe15 alloys is wider than that of the Fe18 alloys. According to **Eq.** Error! Reference source not found. a broader hysteresis loop indicates that the material has a higher HDI stress. Near the yield point, the HDI stress of the Fe15 alloy reaches 620 MPa, whereas the HDI stress of the Fe18 alloy is only 489 MPa. Therefore, the exceptional yield strength of the Fe15 alloy can be attributed to the additional strengthening arising from its significant HDI stress. The hard zones, composed of the BCC phase, impede plastic deformation in the softer regions, resulting in a remarkably high HDI stress for the Fe15 alloy. As the applied strain increases, the HDI stress of both the Fe15 and Fe18 alloys steadily rises. This is likely due to the persistent activation of dislocations, stacking faults, and nano-twins within the hard zones after yielding, which contribute to additional strain hardening capacity.

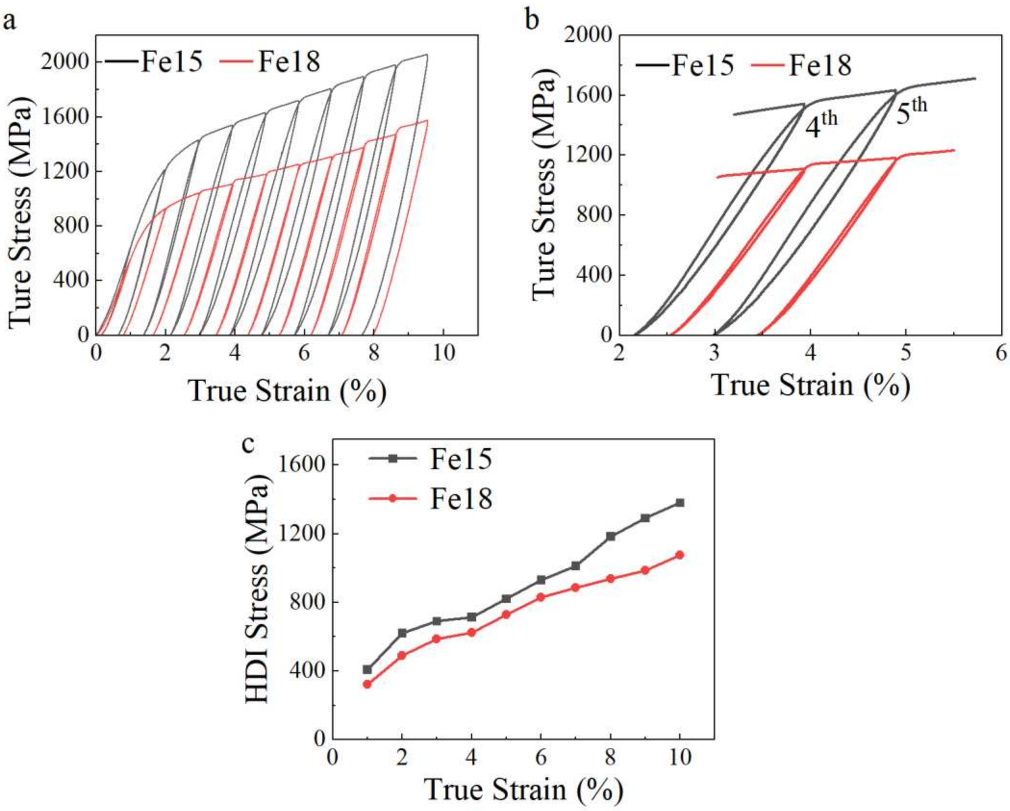


**Fig. 10.** (a) LUR curves of Fe15 and Fe18 alloys; (b) magnified LUR loops taken from (a); (c) evolution of HDI stress as a function of true strain.

To gain an in-depth understanding of the HDI strengthening mechanism, the TEM analysis was performed in this study on the microstructure of near-eutectic alloy following 2% compressive deformation. **Fig. 11** illustrates the microstructural characteristics of the alloy. As shown in **Fig. 11**(a) and (b), during the initial stage of plastic deformation, a high density of dislocations was observed within the γ' phase, while the adjacent B2 phase exhibited a relatively smooth structure with no significant dislocation activity, indicating that plastic deformation initiates in the γ' phase prior to the B2 phase. Furthermore, **Fig. 11**(c) and (d) demonstrate a significant accumulation of GNDs at the interface between the soft γ' phase and the hard B2 phase. This non-uniform distribution of dislocations primarily originates from the mismatch in plastic deformability between the two phases. Under external loading, the more ductile γ′ phase undergoes preferential deformation, while the harder B2 phase constrains dislocation motion near the interface, leading to the gradual accumulation of GNDs). This dislocation pile-up at the interface essentially establishes a strain gradient field from the softer to the harder phase, resulting in a pronounced back stress. This back stress effectively impedes the subsequent movement of dislocations, contributing substantially to the HDI strengthening effect. The findings of this study demonstrate that rational design of a dual-phase microstructure featuring alternating soft and hard domains, particularly one characterized by a continuous and regularly arranged lamellar configuration, enables effective modulation of dislocation activity during deformation and full utilization of the associated back-stress strengthening mechanism. These insights provide valuable guidance for the design of high-performance metallic materials through microstructural optimization.

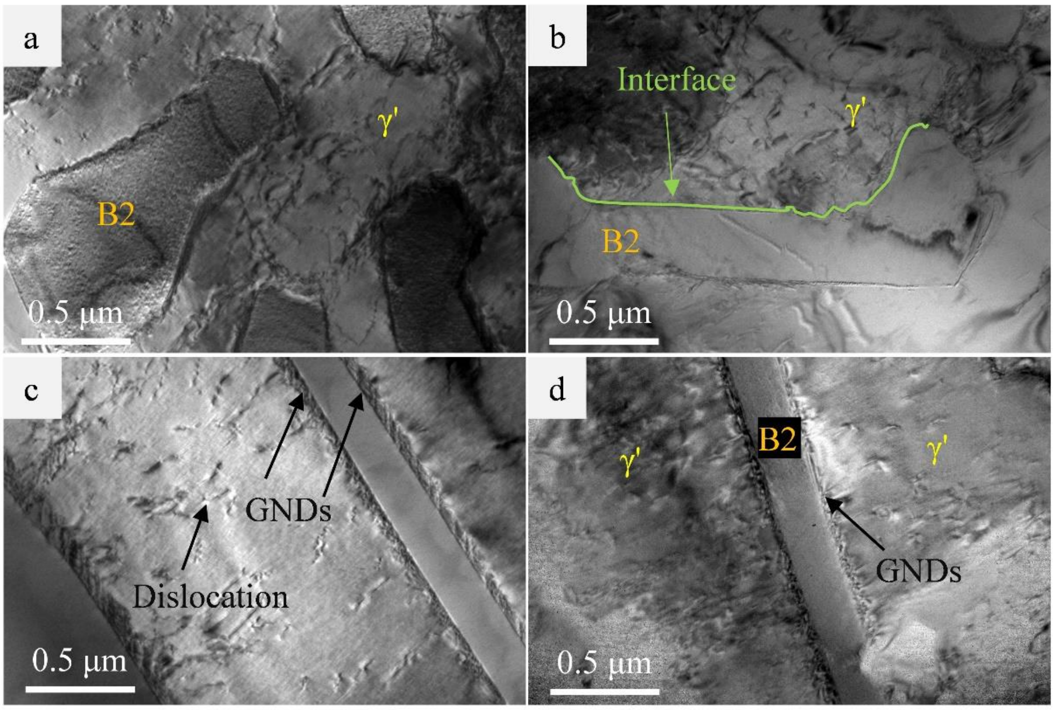


**Fig. 11.** TEM images of Fe15 alloy following deformation at 2% strain. (a) and (b) BF images of heterogeneous structure; (c) and (d) GNDs at boundary between B2 and γ'.

## 5. Conclusions

In this study, a novel Ni-Mn-Ti-Fe-Co alloy system was prepared by arc melting. The alloy simultaneously exhibits TRIP and HDI effects, achieving both high yield strength and excellent ductility. The main conclusions are as follows:

1) With increasing Fe content, the alloys showed a microstructure evolution from dual-phase → hypoeutectic → near-eutectic → hypereutectic microstructures. The orientation relationship of the FCC–B2 interface is determined to be the K–S orientation relationship in the near-eutectic alloy.

2) The $Ni_{35}Mn_{25}Ti_{15}Fe_{15}Co_{10}$ EHEAs demonstrated an excellent combination of strength and ductility with a high yield stress of 1143 MPa and a fracture strain of 21.2%. The stable K–S interface and TRIP effect during deformation contribute to the superior ductility of the Fe15 alloy.

3) All alloys exhibit high yield strength, particularly Fe12 with 1268 MPa, which is attributed to its dual-phase microstructure that enables HDI strengthening. Benefiting from the HDI strengthening, Fe18 alloy maintains a 990 MPa yield strength while achieving exceptional fracture strength of 2417 MPa and a fracture strain of 30.2%.

4) The design of soft/hard eutectic lamellae with stress-induced martensite transformation provides an effective strategy for simultaneously enhancing strength and ductility in EH/MEAs.

## Acknowledgments

This work is financially supported by the National Natural Science Foundation of China (Grant No. 51771044), the Performance subsidy fund for Key Laboratory of Dielectric and Electrolyte Functional Material Hebei (No. 22567627H), 2024 Hebei Provincial doctoral candidate Innovation Ability training funding project (CXZZBS2024179), the Hebei Central Government-Guided Local Science & Technology Development Fund Project (246Z1026G), and the Ministry of Education's “Chunhui Program” Collaborative Research Project (HZKY20220244).

# References


[1] J.W. Yeh, S.K. Chen, S.J. Lin, J.Y. Gan, T.S. Chin, T.T. Shun, C.H. Tsau, S.Y. Chang, Nanostructured high-entropy alloys with multiple principal elements: Novel alloy design concepts and outcomes, Adv. Eng. Mater. 6 (5) (2004) 299-303.

[2] B. Cantor, I.T.H. Chang, P. Knight, A.J.B. Vincent, Microstructural development in equiatomic multicomponent alloys, Mater. Sci. Eng. A. 375-377 (2004) 213-218.

[3] Y. Yuan, J.J. Wang, J. Wei, W.Y. Chen, H.L. Yan, N. Jia, Cu alloying enables superior strength-ductility combination and high corrosion resistance of FeMnCoCr high entropy alloy, J. Alloys Compd. 970 (2024) 172543.

[4] Z.F. He, N. Jia, H.W. Wang, Y. Liu, D.Y. Li, Y.F. Shen, The effect of strain rate on mechanical properties and microstructure of a metastable FeMnCoCr high entropy alloy, Mater. Sci. Eng. A. 776 (2020) 138982.

[5] Q.X. Ma, H.J. Yang, Z. Wang, X.H. Shi, P.K. Liaw, J.W. Qiao, High strength and ductility in partially recrystallized $Fe_{40}Mn_{20}Cr_{20}Ni_{20}$ high-entropy alloys at cryogenic temperature, Microstructures. 2 (3) (2022) 2022015.

[6] T. Wan, Z. Huang, Z. Cheng, M. Zhu, W. Zhu, Z. Li, D. Fu, F. Ren, The effect of chromium content on the corrosion behavior of ultrafine-grained $Cr_x$MnFeCoNi high-entropy alloys in sulfuric acid solution, Microstructures. 3 (2) (2023) 2023014.

[7] J.W. Yeh, Alloy Design Strategies and Future Trends in High-Entropy Alloys, JOM 65 (12) (2013) 1759-1771.

[8] F. Otto, A. Dlouhý, C. Somsen, H. Bei, G. Eggeler, E.P. George, The influences of temperature and microstructure on the tensile properties of a CoCrFeMnNi high-entropy alloy, Acta Mater. 61(15) (2013) 5743-5755.

[9] Z. Tang, O.N. Senkov, C.M. Parish, C. Zhang, F. Zhang, L.J. Santodonato, G. Wang, G. Zhao, F. Yang, P.K. Liaw, Tensile ductility of an AlCoCrFeNi multi-phase high-entropy alloy through hot isostatic pressing (HIP) and homogenization, Mater. Sci. Eng. A. 647 (2015) 229-240.

[10] Y.P. Lu, Y. Dong, S. Guo, L. Jiang, H.J. Kang, T.M. Wang, B. Wen, Z.J. Wang, J.C. Jie, Z.Q. Cao, H.H. Ruan, T.J. Li, A Promising New Class of High-Temperature Alloys: Eutectic High-Entropy Alloys, Sci. Rep. 4 (2014) 6200.

[11] X. Chen, J. Kong, J. Li, S. Feng, H. Li, Q. Wang, Y. Liang, K. Dong, Y. Yang, High-strength AlCoCrFeNi2.1 eutectic high entropy alloy with ultrafine lamella structure via additive manufacturing, Mater. Sci. Eng. A. 854 (2022) 143816.

[12] X. Gao, Y. Lu, B. Zhang, N. Liang, G. Wu, G. Sha, J. Liu, Y. Zhao, Microstructural origins of high strength and high ductility in an $AlCoCrFeNi_{2.1}$ eutectic high-entropy alloy, Acta Mater. 141 (2017) 59-66.

[13] P. Shi, R Liu, Y. Li,Y. Zhong, W. Ren, Z .Shen, T. Zheng, J. Peng, X. Liang, P. Hu, N. Min, Y. Zhang, Y. Ren, P.K. Liaw, D. Raabe, Y. Wang, Hierarchical crack buffering triples ductility in eutectic herringbone high-entropy alloys, Sci. 374 (6557) (2021) 1064-1064.

[14] X. Ye, Z. Cheng, C. Liu, X. Wu, L. Yu, M. Liu, D. Fang, G. Zhao, B. Li, The microstructure and properties of $Fe_{55}Cr_{15}Ni_{(30-x)}Nb_x$ eutectic high-entropy alloys, Mater. Sci. Eng. A. 841 (2022) 143026.

[15] S.R. Reddy, S. Yoshida, U. Sunkari, A. Lozinko, J. Joseph, R. Saha, D. Fabijanic, S. Guo, P.P.

Bhattacharjee, N. Tsuji, Engineering heterogeneous microstructure by severe warm-rolling for enhancing strength-ductility synergy in eutectic high entropy alloys, Mater. Sci. Eng. A. 764 (2019) 138226.

[16] M. Wang, M.X. Huang, Abnormal TRIP effect on the work hardening behavior of a quenching and partitioning steel at high strain rate, Acta Mater. 188 (2020) 551-559.

[17] H.X. Liu, Z.C. Bian, Y.H. Wu, C.X. Xing, X.D. Liu, Y.X. He, Achieving excellent strength-ductility combination in $Co_{60.8-x}Ni_{39.2}Al_x$ eutectic medium-entropy alloys, Mater. Sci. Eng. A. 886 (2023) 145720.

[18] M.S. Mehranpour, M.J. Sohrabi, A. Kalhor, J.H. Lee, A. Heydarinia, H. Mirzadeh, S. Sadeghpour, K. Rodak, M. Nili-Ahmadabadi, R. Mahmudi, H.S. Kim, Exceptional strength-ductility synergy in the novel metastable FeCoCrNiVSi high-entropy alloys via tuning the grain size dependency of the transformation-induced plasticity effect, Int. J. Plast. 182 (2024) 104115.

[19] Z.M. Li, K.G. Pradeep, Y. Deng, D. Raabe, C.C. Tasan, Metastable high-entropy dual-phase alloys overcome the strength-ductility trade-off, Nature 534 (7606) (2016) 227-230.

[20] X.L. Wu, M.X. Yang, F.P. Yuan, G.L. Wu, Y.J. Wei, X.X. Huang, Y.T. Zhu, Heterogeneous lamella structure unites ultrafine-grain strength with coarse-grain ductility, Proc. Natl. Acad. Sci. U.S.A. 112 (47) (2015) 14501-14505.

[21] Y. Liu, Y. Cao, Q. Mao, H. Zhou, Y. Zhao, W. Jiang, Y. Liu, J.T. Wang, Z. You, Y. Zhu, Critical microstructures and defects in heterostructured materials and their effects on mechanical properties, Acta Mater. 189 (2020) 129-144.

[22] M.X. Yang, Y. Pan, F.P. Yuan, Y.T. Zhu, X.L. Wu, Back stress strengthening and strain hardening in gradient structure, Mater. Res. Lett. 4 (3) (2016) 145-151.

[23] Z. He, N. Jia, H. Yan, Y. Shen, M. Zhu, X. Guan, X. Zhao, S. Jin, G. Sha, Y. Zhu, C.T. Liu, Multi-heterostructure and mechanical properties of N-doped FeMnCoCr high entropy alloy, Int. J. Plast. 139 (2021) 102965.

[24] Q. Pan, L. Zhang, R. Feng, Q. Lu, K. An, A.C. Chuang, J.D. Poplawsky, P.K. Liaw, L. Lu, Gradient cell–structured high-entropy alloy with exceptional strength and ductility, 374 (6570) (2021) 984-989.

[25] Y.T. Sun, X. Kong, Z.B. Wang, Superior mechanical properties and deformation mechanisms of a 304 stainless steel plate with gradient nanostructure, Int. J. Plast. 155 (2022) 103336.

[26] Q. Pan, M. Yang, R. Feng, A.C. Chuang, K. An, P.K. Liaw, X. Wu, N. Tao, L. Lu, Atomic faulting induced exceptional cryogenic strain hardening in gradient cell–structured alloy, 382 (6667) (2023) 185-190.

[27] S. Jiang, R.L. Peng, K. Máthis, H.-L. Yan, G. Farkas, Z. Hegedues, U. Lienert, J. Moverare, X. Zhao, L. Zuo, N. Jia, Y.-D. Wang, Shear banding-induced (c plus a) slip enables unprecedented strength-ductility combination of laminated metallic composites, J. Mater. Sci. Technol. 110 (2022) 260-268.

[28] G. Li, J. Jiang, H. Ma, R. Zheng, S. Gao, S. Zhao, C. Ma, K. Ameyama, B. Ding, X. Li, Superior strength–ductility synergy in three-dimensional heterogeneous-nanostructured metals, Acta Mater. 256 (2023) 119143.

[29] J.Y. He, H. Wang, H.L. Huang, X.D. Xu, M.W. Chen, Y. Wu, X.J. Liu, T.G. Nieh, K. An, Z.P. Lu, A precipitation-hardened high-entropy alloy with outstanding tensile properties, Acta Mater. 102 (2016) 187-196.

[30] Y.J. Liang, L.J. Wang, Y.R. Wen, B.Y. Cheng, Q.L. Wu, T.Q. Cao, Q. Xiao, Y.F. Xue, G. Sha, Y.D. Wang, Y. Ren, X.Y. Li, L. Wang, F.C. Wang, H.N.A. Cai, High-content ductile coherent nanoprecipitates achieve ultrastrong high-entropy alloys, Nat. Commun. 9 (2018) 4063.

[31] J.B. Seol, J.W. Bae, J.G. Kim, H. Sung, Z. Li, H.H. Lee, S.H. Shim, J.H. Jang, W.-S. Ko, S.I. Hong, H.S. Kim, Short-range order strengthening in boron-doped high-entropy alloys for cryogenic applications, Acta Mater. 194 (2020) 366-377.

[32] N. Shah, M.R. Rahul, S. Bysakh, G. Phanikumar, Microstructure stability during high temperature deformation of CoCrFeNiTa eutectic high entropy alloy through nano-scale precipitation, Mater. Sci. Eng. A. 824 (2021) 141793.

[33] T. Xiong, S. Zheng, J. Pang, X. Ma, High-strength and high-ductility AlCoCrFeNi2.1 eutectic high-entropy alloy achieved via precipitation strengthening in a heterogeneous structure, Scr. Mater. 186 (2020) 336-340.

[34] Y. Jia, Z. Wang, Q. Wu, F. He, J. Li, J. Wang, Enhancing the yield strength of Ni–Co–Cr–Fe–Al as-cast hypoeutectic high-entropy alloys by introducing γ′ precipitation, Mater. Sci. Eng. A. 858 (2022) 144190.

[35] T. Xiong, W.F. Yang, S.J. Zheng, Z.R. Liu, Y.P. Lu, R.F. Zhang, Y.T. Zhou, X.H. Shao, B. Zhang, J. Wang, F.X. Yin, P.K. Liaw, X.L. Ma, Faceted Kurdjumov-Sachs interface-induced slip continuity in the eutectic high-entropy alloy, $AlCoCrFeNi_{2.1}$, J. Mater. Sci. Technol. 65 (2021) 216-227.

[36] G. Kurdjumow, G. Sachs, Über den Mechanismus der Stahlhärtung, Z. Angew. Phys. 64 (5-6) (1930) 325-343.

[37] R. Zhu, J. Yuan, Z. Wang, X. Shi, H. Yang, J. Qiao, "Double-yielding" behavior and progressive β → α → twins transformation in a Ti-based metallic glass matrix composite, Scr. Mater. 218 (2022) 114838.

[38] L. Zhang, S. Chen, H.M. Fu, H. Li, Z.W. Zhu, H.W. Zhang, Z.K. Li, A.M. Wang, H.F. Zhang, Tailoring modulus and hardness of in-situ formed β-Ti in bulk metallic glass composites by precipitation of isothermal ω-Ti, Mater. Des. 133 (2017) 82-90.

[39] G.A. Sun, X.L. Wang, Y.D. Wang, W.C. Woo, H. Wang, X.P. Liu, B. Chen, Y.Q. Fu, L.S. Sheng, Y. Ren, In-situ high-energy synchrotron X-ray diffraction study of micromechanical behavior of multiple phases in $Ni_{47}Ti_{44}Nb_9$ shape memory alloy, Mater. Sci. Eng. A. 560 (2013) 458-465.

[40] E. Ma, X.L. Wu, Tailoring heterogeneities in high-entropy alloys to promote strength-ductility synergy, Nat. Commun. 10 (2019) 5623.

[41] H.Z. Pan, Y. Yuan, Y.L. Yang, Z.F. He, S. Jiang, M.W. Zhu, W.Y. Chen, N. Jia, Multi-scaled heterostructure enables superior strength-ductility combination of a CoCrFeMnN compositionally-complex alloy, J. Mater. Sci. Technol. 222 (2025) 82-93.